The Effect of Temperature on the Viscoelastic Response of Semicrystalline Polymers

A. D. Drozdov, S. Agarwal, R. K. Gupta

Department of Chemical Engineering, West Virginia University, P.O. Box 6102, Morgantown, West Virginia 26506, USA

Received 2 June 2003; accepted 1 March 2004
DOI 10.1002/app.20656
Published online in Wiley InterScience (www.interscience.wiley.com).

ABSTRACT: Three series of isothermal torsion relaxation tests were performed at various temperatures ranging from room temperature to $T = 120°C$ on isotactic polypropylene, low-density polyethylene, and linear low-density polyethylene. Constitutive equations are derived for the viscoelastic behavior of a semicrystalline polymer at small strains. A polymer is treated as an equivalent network of strands bridged by temporary junctions (entanglements, physical crosslinks on the surfaces of crystallites, and lamellar blocks). The network is thought of as an ensemble of mesoregions with various activation energies for detachment of active strands from their junctions. The time-dependent response of the ensemble reflects thermally induced rearrangement of strands (separation of active strands from temporary junctions and merging of dangling strands with the network). Stress–strain relations are developed by using the laws of thermodynamics. The governing equations involve five adjustable parameters that are found by fitting the experimental data. This study focuses on the influence of temperature and crystalline morphology of polyolefins on the material parameters in the constitutive relations. © 2004 Wiley Periodicals, Inc. J Appl Polym Sci 94: 9–23, 2004

Key words: polyethylene; polypropylene; viscoelastic properties; thermal properties

INTRODUCTION

This article is concerned with the effect of temperature on the viscoelastic behavior of semicrystalline polymers at isothermal deformations with small strains. The experimental part focuses on the time-dependent response of injection-molded isotactic polypropylene (iPP), low-density polyethylene (LDPE), and linear low-density polyethylene (LLDPE) in torsion relaxation tests. The choice of these polymers for the investigation is explained by (1) their numerous industrial applications (oriented films for packaging, reinforcing fibers, nonwoven fabrics, pipes, wire coatings, fuel tanks, etc.), and (2) variety of crystalline morphologies (ranging from monoclinic spherulites in iPP to orthorhombic structures in LDPE and LLDPE) and molecular architectures in the amorphous phase (ranging from highly branched chains in LDPE to linear chains with relatively short branches in LLDPE) that noticeably affect their mechanical and physical properties.

Isotactic polypropylene is a semicrystalline polymer containing the three following crystallographic forms: monoclinic α crystallites, hexagonal β structures, orthorhombic γ polymorphs, and smectic mesophase.[1] At cooling of the melt with the rates typical of the injection-molding process, α crystallites and smectic mesophase are mainly developed, whereas β and γ polymorphs are observed as minority components.[2,3] A unique feature of the crystalline morphology of iPP is the lamellar cross-hatching: development of transverse lamellae oriented in the direction perpendicular to the direction of radial lamellae.[1,4] The characteristic size of spherulites in injection-molded specimens is estimated as 100–200 μm.[2,5] The spherulites consist of crystalline lamellae with thicknesses of 10–20 nm.[4,5]

Polyethylene reveals three different crystallographic forms: monoclinic, hexagonal, and orthorhombic. Monoclinic and hexagonal structures are produced by polymerization under high pressure (over 400 MPa) and high temperature only,[6,7] whereas in injection-molded samples, orthorhombic structures are mainly formed.

Linear chains in LDPE have a large number of long side branches that prevent macromolecules from packing closely in crystallites and result in a wide distribution of sizes of spherulites. The average radius of spherulites equals 3–12 μm.[8] The spherulites are formed by lamellae stacks with lamellar thicknesses ranging from 8 to 12 nm.[9] There data were confirmed in [10], where an average lamellar thickness of 11.5 nm was found, but were argued in [11], where an average

Correspondence to: A. D. Drozdov (Aleksey.Drozdov@mail.wvu.edu).

Contract grant sponsor: West Virginia Research Challenge Grant Program.

thickness of 6.5 nm was reported. The average size of lamellae and their curvature, as well as the type of their organization into spherulites, are strongly affected by crystallization conditions, molecular weight, and degree of chain branching.[12]

LLDPE is a random copolymer produced by polymerization of ethylene in the presence of alkenes (butene, octene, octadecene, hexene, etc.). The average distance between short branches along the main chain is about 7 nm.[12] This value perfectly agrees with the average segment length found in [13] for metallocene-catalyzed LLDPE (under the assumptions that sidechains are segregated from crystallites, and only a small amount of them may be included into crystallites as defects[6]). The histograms reported in [13] reveal a wide distribution of segment lengths, with a relatively high probability of segments ranging up to 30 nm (which, in turn, implies a wide distribution of lamellar thicknesses in LLDPE). The average radius of crystallites is strongly affected by the content of short-chain branches (composed mainly of butyl side groups with minor amounts of ethyl, methyl, and hexyl side groups[12]), and it changes from 2.5 to 12 μm depending on the crystallization conditions.[8] The average lamellar thickness ranges from 8.5 to 10 nm.[8]

In semicrystalline polymers, the amorphous phase is located (1) between spherulites, (2) inside spherulites in liquid pockets between lamellar stacks,[14] and (3) between lamellae in lamellar stacks. It consists of (1) relatively mobile chains between spherulites and in liquid pockets, and (2) severely restricted chains between lamellae in lamellar stacks (the so-called restrained chains[15] or rigid amorphous fraction[14]: part of the amorphous phase whose molecular mobility is substantially suppressed by surrounding crystallites).

In the past decade, the viscoelastic response of isotactic polypropylene has been investigated in [16–18, 20–23], to mention a few. The time-dependent behavior of polyethylene was analyzed in [24–35]. Although viscoelasticity of solid polyolefins was investigated in a number of publications, a comparative study of the influence of temperature on the time-dependent response of polyethylene and polypropylene has not yet been performed.

The objective of this work is twofold:

1. To report experimental data in uniaxial torsion relaxation tests on isotactic polypropylene, LDPE and LLDPE in the interval of temperatures from 30 to 120°C.
2. To derive constitutive equations for the viscoelastic response of semicrystalline polymers and to determine adjustable parameters in the stress–strain relations by fitting the observations.

Our purpose is to assess the effect of temperature on the time-dependent behavior of semicrystalline polymers in terms of the model parameters and to establish correlations between their crystalline morphology and the mechanical response.

To develop a constitutive model with a relatively small number of material constants, we applied a method of homogenization.[36] According to this approach, a sophisticated microstructure of a semicrystalline polymer is replaced by a single phase, whose response captures essential features of the time-dependent behavior of the polymer. Following [20, 22, 37, 38], we treat the equivalent phase as a network of macromolecules connected by temporary junctions (entanglements, physical crosslinks on the surfaces of crystallites, and fringed micellar crystals serving as the multifunctional junctions[37]).

To simplify the derivation of stress–strain relations, we assume the network to be incompressible. This hypothesis is confirmed by experimental data,[39] which show that LLDPE is practically incompressible under tension with the elongation ratios up to 2.5.

With reference to the theory of transient networks,[40–43] the viscoelastic response of a semicrystalline polymer is associated with separation of active strands from temporary junctions and merging of dangling strands with the network. Rearrangment of strands in the network is thought of as a thermally activated process: an end of an active strand detaches from a junction and a free end of a dangling strand captures a nearby junction at random instants, when these strands are thermally activated.

The network is assumed to be strongly heterogeneous. Its spatial inhomogeneity is attributed to interactions between amorphous regions and crystalline lamellae with various lengths and thicknesses, as well as to local density fluctuations in the amorphous phase. The equivalent network is treated as an ensemble of mesoregions (MRs) with various activation energies for detachment of active strands from their junctions. Following [44], the following two types of MRs are distinguished: (1) active domains, where strands separate from their junctions as they are thermally agitated (these MRs are associated with a mobile part of the amorphous phase), and (2) passive domains, where detachment of strands from their junctions is prevented (these MRs reflect the response of a part of the amorphous phase whose mobility is severely restricted by surrounding crystallites).

The exposition is organized as follows. We begin with reporting the experimental data in torsional relaxation tests. Afterwards, stress–strain relations are developed for an arbitrary three-dimensional deformation of a semicrystalline polymer. The constitutive equations are simplified for torsion of a cylinder and plane bending of a beam, the deformation modes that correspond to torsional relaxation tests and bending creep tests. Adjustable parameters in the governing equations are found by fitting the observations in

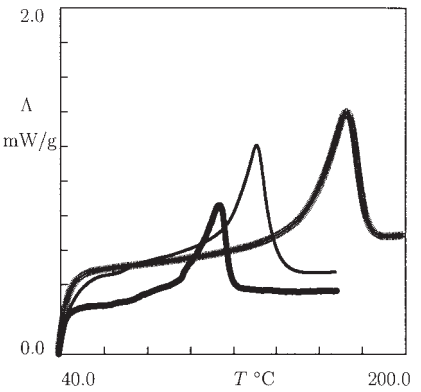

Figure 1 The exothermic heat flow Λ versus temperature T. Symbols: observations on LDPE (thick line), LLDPE (thin line), and iPP (asterisks).

relaxation tests. After a brief discussion of our finding, the governing equations are verified by comparison of experimental data in bending creep tests with results of numerical simulation. Finally, some concluding remarks are formulated.

EXPERIMENTAL

Isotactic polypropylene PP 1012 (density, 0.906 g/cm^3; melt flow rate, 1.2 g/10 min) was purchased from BP Amoco Polymers, Inc. (Alpharetta, GA) LDPE PE 1020 (density, 0.923 g/cm^3; melt flow rate, 2.0 g/10 min) was purchased from Huntsman Corp. (Salt Lake City, UT). LLDPE Petrothene GA 584 (density, 0.929 g/cm^3; melt flow rate, 105 g/10 min) was supplied by Equistar Chemicals (Columbus, OH).

Granules were dried at the temperature T = 100°C for 12 h before molding. ASTM specimens for mechanical tests with length of 45.5 mm, width of 13.0 mm, and thickness of 3.0 mm were molded in an injection-molding machine (Battenfeld 1000/315 CDC, Battenfeld).

To evaluate the degree of crystallinity κ_c, differential scanning calorimetry (DSC) measurements were performed by using DSC 910S apparatus (TA Instruments). The calorimeter was calibrated with indium as a standard. Specimens with weights in the range from 13 to 26 mg were tested with a heating rate of 10 K/min from room temperature to 200°C. The DSC traces of three polymers are depicted in Figure 1. The graphs are similar to those reported by other researchers for LDPE and LLDPE,[11,27] and iPP.[1,45,46] The melting temperatures T_m were determined as the points corresponding to the peaks on melting curves. The specific enthalpy of melting ΔH_m was calculated from the areas of endotherms by using a standard procedure. The degree of crystallinity was determined as the ratio of the enthalpy of melting to the enthalpy of fusion for a perfectly crystalline polymer (209 J/g for polypropylene and 293 J/g for polyethylene[47]). Our findings are listed in Table I.

TABLE I
Melting Temperatures T_m and Degrees of Crystallinity κ_c of Semicrystalline Polymers

Polymer	T_m (°C)	κ_c (%)
iPP	172.1	44.3
LDPE	113.2	19.4
LLDPE	130.8	34.2

To analyze the crystalline morphology of polymer, X-ray diffraction tests were performed on bulk samples by using Rugaku D-max B diffractometer with CuK$_\alpha$ radiation (λ = 1.54 Å) generated by a tube with a voltage of 40 kV and a current of 30 mA. The Bragg scattering angle ranged from 2θ = 3 to 2θ = 40° with the step of 0.06°. The diffraction spectra of LDPE and LLDPE are analogous to those previously reported in the literature,[48,49] and we do not present them for the sake of brevity. The WAXS profiles of polyethylenes reveal only two peaks: an orthorhombic (110) peak near 2θ = 21°, and a triclinic peak (200) near 2θ = 24°. The X-ray diffraction pattern of iPP depicted in Figure 2 is also similar to conventional WAXS diagrams. The only difference is that we observed a rather narrow β(300) peak. This peak was absent in the diagrams presented in [1, 46], but it was reported in [50, 51], to mention a few.

Relaxation tests were performed by using rheometric scientific mechanical spectrometer RMS-800 in rectangular torsion mode. To avoid the effect of physical aging, mechanical tests were carried out a few days after preparation of samples.

The series of relaxation experiments on iPP consisted of 10 tests at the temperatures T = 30, 40, 50, 60, 70, 80, 90, 100, 110, and 120°C. The series of experiments on LDPE consisted of eight tests at the temperatures T = 30, 40, 50, 60, 70, 80, 90, and 100°C. The series of experiments on LLDPE consisted of nine tests

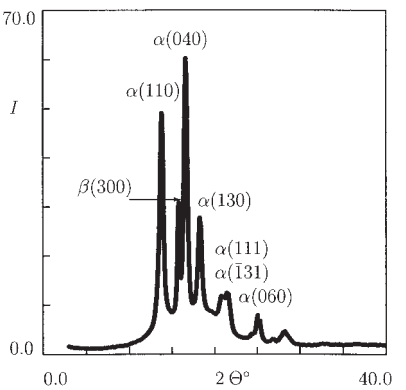

Figure 2 X-ray diffraction patterns of iPP: intensity I (in 10^3 of counts) versus the Bragg angle 2θ.

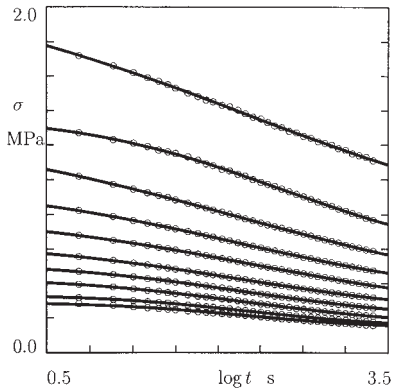

Figure 3 The stress σ versus time t. Circles: experimental data on iPP in relaxation tests at the temperatures $T = 30$, 40, 50, 60, 70, 80, 90, 100, 110, and 120°C, from top to bottom, respectively. Solid lines: results of numerical simulation.

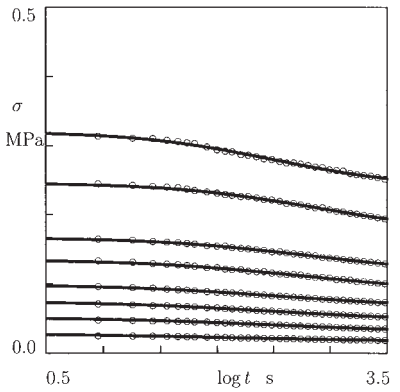

Figure 4 The stress σ versus time t. Circles: experimental data on LDPE in relaxation tests at the temperatures $T = 30$, 40, 50, 60, 70, 80, 90, and 100°C, from top to bottom, respectively. Solid lines: results of numerical simulation.

at the temperatures $T = 30$, 40, 50, 60, 70, 80, 90, 100, and 110°C. All tests were performed below the melting temperatures of the polymers under consideration. In the relaxation tests, the temperature in the chamber was controlled with a standard thermocouple. It was found that the temperature remained constant within the accuracy of ± 0.5°C.

In each relaxation test, a specimen was equilibrated at a given temperature T (for 10 min). Afterwards, the specimen was loaded up to a given twist angle $\vartheta^0 = 5.0 \times 10^{-4}$ rad for iPP and $\vartheta^0 = 1.0 \times 10^{-3}$ rad for LDPE and LLDPE within 4 s. The twist angle was preserved constant during the relaxation time $t_r = 40$ min, and the torque was measured by using a standard load cell. The shear stress σ was determined as the ratio of the torque multiplied by the length of the specimen to its cross-sectional moment of inertia, see eq. (22) below. At each temperature T, at least two relaxation tests were carried out on different samples.

The shear stress σ is plotted versus the logarithm ($\log = \log_{10}$) of time t in Figure 3 for iPP, in Figure 4 for LDPE, and in Figure 5 for LLDPE. The initial instant $t = 0$ corresponds to the beginning of the relaxation process. These figures demonstrate that the decrease in stress is rather pronounced at relatively low temperatures (30 and 40°C), but it becomes less substantial when the temperature T increases. At high temperatures (above 100°C), the relaxation curves are practically parallel to the abscissa axis.

Our aim now is to derive constitutive equations that adequately describe the experimental data depicted in Figures 3–5.

CONSTITUTIVE EQUATIONS

A semicrystalline polymer is treated as a transient network of strands bridged by temporary junctions (entanglements between chains in the amorphous regions, physical crosslinks at the surfaces of crystallites, and lamellar blocks).

The time-dependent behavior of a semicrystalline polymer is modeled within the concept of transient networks. Active strands (whose ends are connected to contiguous junctions) are assumed to separate from temporary junctions at random times when these strands are thermally activated. An active strand whose end detaches from a junction is transformed into a dangling strand. A dangling strand returns into the active state when its free end captures a nearby junction at a random instant.

Detachment of active strands from their junctions and merging of dangling strands with the network are thought of as thermally activated processes. Separation of an active strand from a junction is determined by its activation energy v. With reference to [52], we suppose that for an active strand with activation energy v, the probability $q(v)$ for its transition into the

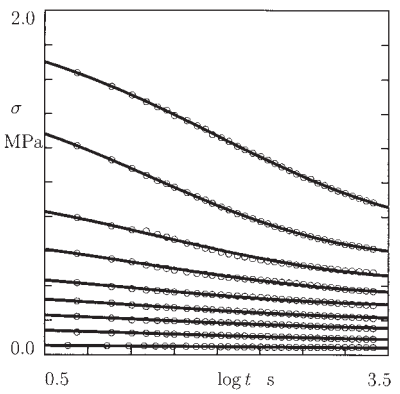

Figure 5 The stress σ versus time t. Circles: experimental data on LLDPE in relaxation tests at the temperatures $T = 30$, 40, 50, 60, 70, 80, 90, 100, and 110°C, from top to bottom, respectively. Solid lines: results of numerical simulation.

dangling state is described by the exponential statistics

$$q(v) = \exp(-\beta v) \quad (v \geq 0), \quad q(v) = 0 \quad (v < 0) \quad (1)$$

where β is a material constant, which is assumed to be independent of temperature T.

γ is the attempt rate (the average number of activation events for an active strand per unit time). The rate of detachment Γ is defined as the product of the attempt rate γ by the probability of transition into the dangling state driven by thermal fluctuations. It follows from eq. (1) that for any $v \geq 0$,

$$\Gamma(v) = \gamma \exp(-\beta v)$$

Without loss of generality, we set $\beta = 1$ in this equality, which implies that the activation energies of strands are measured in units of β^{-1},

$$\Gamma(v) = \gamma \exp(-v) \quad (v \geq 0) \quad (2)$$

An equivalent network of strands is modeled as an ensemble of mesoregions with various activation energies for detachment of active strands from their junctions. Two types of mesoregions are distinguished: passive and active. In passive MRs, interchain interaction prevents detachment of strands from the network, which implies that all junctions in these domains are permanent. In active MRs, active strands separate from temporary junctions and dangling strands merge with the network at random times.

N_a is the number of active strands in active MRs; N_p is the number of strands connected to the network in passive MRs, and

$$N = N_a + N_p \quad (3)$$

the average number of active strands per unit mass of a polymer. The ensemble of mesoregions with various activation energies v is characterized by the concentration of active MRs

$$\kappa = \frac{N_a}{N} \quad (4)$$

and the distribution function $p_a(v)$ for active strands in active MRs with various activation energies. The quantity $p_a(v)$ equals the ratio of the number $\nu_a(v)$ of active strands in active mesodomains with energy v to the total number active strands N_a,

$$p_a(v) = \frac{\nu_a(v)}{N_a} \quad (5)$$

At small deformations, the total number of active strands N, the concentration of active mesodomains κ, and the distribution function $p_a(v)$ are independent of mechanical factors, but they are strongly affected by temperature T.

In what follows, constitutive equations will be derived for an arbitrary distribution function $p_a(v)$. To fit experimental data, we adopt the random energy model[53] with the quasi-Gaussian distribution function

$$p_a(v) = p_0 \exp\left[-\frac{(v - V)^2}{2\Sigma^2}\right] \quad (v \geq 0),$$

$$p(v) = 0 \quad (v < 0) \quad (6)$$

where V is an analog of the average energy for rearrangement of strands, Σ is an analog of the standard deviation of activation energies, and the coefficient p_0 is determined from the condition

$$\int_0^\infty p_a(v)\, dv = 1 \quad (7)$$

An ensemble of active mesodomains is characterized by the function $n_a(t, \tau, v)$ that equals the number (per unit mass) of active strands at time $t \geq 0$ belonging to active MRs with activation energy v that have last rearranged before instant $\tau \in [0, t]$. In particular, $n_a(t, t, v)$ is the number (per unit mass) of active strands in active MRs with potential energy v at time $t \geq 0$,

$$n_a(t, t, v) = \nu_a(v) \quad (8)$$

The amount $\varphi(\tau, v)d\tau$, where

$$\varphi(\tau, v) = \frac{\partial n_a}{\partial \tau}(t, \tau, v)\big|_{t=\tau} \quad (9)$$

equals the number (per unit mass) of dangling strands in active MRs with activation energy v that merge with the network within the interval $[\tau, \tau + d\tau]$, and the quantity

$$\frac{\partial n_a}{\partial \tau}(t, \tau, v)\, d\tau$$

is the number of these strands that have not detached from their junctions during the interval $[\tau, t]$. The number (per unit mass) of strands in active MRs that separate (for the first time) from the network within the interval $[t, t + dt]$ reads

$$-\frac{\partial n_a}{\partial t}(t, 0, v)\, dt$$

and the number (per unit mass) of strands in active MRs that merged with the network during the interval $[\tau, \tau + d\tau]$ and, afterwards, separate from the network within the interval $[t, t + dt]$ is given by

$$-\frac{\partial^2 n_a}{\partial t \partial \tau}(t, \tau, v)\, dt\, d\tau$$

The rate of detachment Γ equals the ratio of the number of active strands that separate from the network per unit time to the current number of active strands. Applying this definition to active strands that are rearranged for the first time within the interval $[t, t + dt]$ and to those that have been previously rearranged during the interval $[\tau, \tau + d\tau]$, we arrive at the differential equations

$$\frac{\partial n_a}{\partial t}(t, 0, v) = -\Gamma(v) n_a(t, 0, v),$$

$$\frac{\partial^2 n_a}{\partial t \partial \tau}(t, \tau, v) = -\Gamma(v)\frac{\partial n_a}{\partial \tau}(t, \tau, v)$$

Integration of these equations with initial conditions (8) (where we set $t = 0$) and (9) implies that

$$n_a(t, 0, v) = \kappa N p_a(v) \exp[-\Gamma(v) t]$$

$$\frac{\partial n_a}{\partial \tau}(t, \tau, v) = \kappa N p_a(v) \Gamma(v) \exp[-\Gamma(v)(t - \tau)] \quad (10)$$

For a detailed derivation of eqs. (10), the reader is referred to [23].

An active strand is thought of as an incompressible linear elastic medium with the strain energy

$$w = \frac{1}{2}\mu \hat{e}' : \hat{e}'$$

where μ is an average rigidity per strand, $\hat{e}$ is the strain tensor for transition from the natural (stress-free) state of a strand to its deformed state, and the prime stands for the deviatoric component of a tensor.

For strands belonging to passive MRs, the stress-free configuration coincides with the reference configuration of the network. This implies that the tensor $\hat{e}'$ equals the deviatoric component $\hat{\epsilon}'$ of the macrostrain tensor $\hat{\epsilon}$. Multiplying the mechanical energy of a strand by the number of strands in passive MRs, we find the strain energy of mesodomains where rearrangement of strands is prevented by surrounding lamellae,

$$W_p(t) = \frac{1}{2}\mu N_p \hat{\epsilon}'(t) : \hat{\epsilon}'(t) \quad (11)$$

With reference to [43], we suppose that stress in a dangling strand totally relaxes before the strand captures a nearby junction. This implies that the stress-free configuration of an active strand coincides with the deformed configuration of the network at the instant when the strand attaches to the network. This means that for active strands that have not rearranged before instant $t \geq 0$, the strain $\hat{e}'$ reads

$$\hat{e}(t, 0) = \hat{\epsilon}'(t)$$

whereas for active strands that have last rearranged within the interval $[\tau, \tau + d\tau]$, the strain $\hat{e}'$ is given by

$$\hat{e}'(t, \tau) = \hat{\epsilon}'(t) - \hat{\epsilon}'(\tau)$$

Summing the strain energies of active strands belonging to mesoregions with various potential energies v that rearranged at various instants $\tau \in [0, t]$, we find the strain energy of active MRs,

$$W_a(t) = \frac{1}{2}\mu \int_0^\infty \left[n_a(t, 0, v)\hat{\epsilon}'(t) : \hat{\epsilon}'(t) + \int_0^t \frac{\partial n_a}{\partial \tau} \times (t, \tau, v)(\hat{\epsilon}'(t) - \hat{\epsilon}'(t)) : (\hat{\epsilon}'(t) - \hat{\epsilon}'(t))\, d\tau \right] dv \quad (12)$$

Neglecting the energy of interaction between strands (this energy is taken into account in terms of the incompressibility condition for the network), we calculate the strain energy per unit mass of a semicrystalline polymer as the sum of the strain energies of strands in active and passive MRs,

$$W(t) = W_a(t) + W_p(t)$$

It follows from this equality and eqs. (9)–(12) that the derivative of the function $W(t)$ with respect to time is given by

$$\frac{dW}{dt}(t) = \hat{A}'(t) : \frac{d\hat{\epsilon}'}{dt}(t) - B(t) \quad (13)$$

where

$$\hat{A}(t) = \mu\left[N\hat{\epsilon}(t) - \int_0^\infty dv \int_0^t \frac{\partial n_a}{\partial \tau}(t, \tau, v)\hat{\epsilon}(\tau)\, dt \right] \quad (14)$$

$$B(t) = \frac{1}{2}\mu \int_0^\infty \Gamma(v)\, dv \left[n_a(t, 0, v)\hat{\epsilon}'(t) : \hat{\epsilon}'(t) + \int_0^t \frac{\partial n_a}{\partial \tau} \times (t, \tau, v)(\hat{\epsilon}'(t) - \hat{\epsilon}'(\tau)) : (\hat{\epsilon}'(t) - \bar{\epsilon}'(\tau))\, d\tau \right] \quad (15)$$

Equation (15) implies that the function $B(t)$ is nonnegative: $\Gamma(v)$ is positive as the rate of detachment of strands from temporary junctions, $n_a(0, t, v)$ and $\partial n_a/\partial\tau(t, \tau, v)$ are nonnegative as concentrations of active strands in mesoregions with various activation energies, whereas the convolution of a tensor with itself is positive for any nonzero tensor.

For isothermal deformation of an incompressible medium, the Clausius–Duhem inequality reads

$$Q(t) = -\frac{dW}{dt}(t) + \frac{1}{\rho}\hat{\sigma}'(t) : \frac{d\hat{\epsilon}'}{dt}(t) \geq 0$$

where Q is internal dissipation per unit mass, ρ is density, and $\hat{\sigma}'$ is the deviatoric component of the stress tensor $\hat{\sigma}$. Substitution of eq. (13) into this equality implies that

$$\rho Q(t) = [\hat{\sigma}'(t) - \rho\hat{A}'(t)] : \frac{d\hat{\epsilon}'}{dt}(t) + \rho B(t) \geq 0 \quad (16)$$

As the function $B(t)$ is nonnegative, the dissipation inequality (16) is satisfied for an arbitrary deformation program, provided that the expression in square brackets vanishes. This condition, together with eqs. (10) and (14), results in the stress–strain relation

$$\hat{\sigma}(t) = -P(t)\hat{I} + 2G\left[\hat{\epsilon}'(t) - \kappa\int_0^\infty \Gamma(v)p_a(v)\,dv \times \int_0^t \exp(-\Gamma(v)(t-\tau))\hat{\epsilon}'(\tau)\,d\tau\right] \quad (17)$$

where P is an unknown pressure, $\hat{I}$ is the unit tensor, and $G = \frac{1}{2}\rho\mu N$ is an analog of the elastic modulus. The first term on the right-hand side of eq. (17) arises due to the incompressibility condition.

For an arbitrary three-dimensional deformation with small strains, the viscoelastic response of a semicrystalline polymer is determined by eqs. (2), (6), and (17). These equations involve five material constants to be found by fitting observations:

1. the modulus G,
2. the concentration of active MRs κ,
3. the attempt rate for rearrangement of strands γ,
4. the average activation energy for rearrangement V,
5. the standard deviation of activation energies Σ.

Our aim now is to simplify the stress–strain relations for torsion of a cylindrical specimen and bending of a beam.

TORSION OF A CYLINDER

We begin with torsion of a cylinder driven by a torque $M(t)$ applied to its edges. The axial force equals zero, and the lateral surface of the cylinder is traction-free. In the initial state, points of the cylinder refer to cylindrical coordinates $\{r, \phi, z\}$ with unit vectors $\bar{e}_r$, $\bar{e}_\phi$, and $\bar{e}_z$.

Torsion of a cylinder is described by the following equations:

$$R = r, \quad \Phi = \phi + \alpha z, \quad Z = z \quad (18)$$

where $\{R, \Phi, Z\}$ are cylindrical coordinates in the deformed state, and $\alpha(t)$ denotes twist angle per unit length. It follows from eq. (18) that the strain tensor $\hat{\epsilon}$ reads

$$\hat{\epsilon} = \frac{1}{2}\alpha r(\bar{e}_\phi\bar{e}_z + \bar{e}_\phi\bar{e}_z) \quad (19)$$

Substitution of expression (19) into eq. (17) implies that

$$\hat{\sigma} = \sigma_{\phi z}(\bar{e}_\phi\bar{e}_z + \bar{e}_\phi\bar{e}_z)$$

where

$$\sigma_{\phi z}(t) = Gr\left[\alpha(t) - \kappa\int_0^\infty \Gamma(v)p_a(v)\,dv \times \int_0^t \exp(-\Gamma(v)(t-\tau))\alpha(\tau)\,d\tau\right] \quad (20)$$

The stress tensor $\hat{\sigma}$ satisfies the equilibrium equations inside the cylinder and the boundary conditions on its lateral surface. The only boundary condition on the edges of the cylinder reads

$$M(t) = \int_S \sigma_{\phi z} r^2\,dr\,d\phi \quad (21)$$

where S is a domain occupied by the cross section. Combining eqs. (20) and (21), we find that

$$M(t) = \frac{GJ}{l}\left[\vartheta(t) - \kappa\int_0^\infty \Gamma(v)p_a(v)\,dv \times \int_0^t \exp(-\Gamma(v)(t-\tau))\vartheta(\tau)\,d\tau\right]$$

where

$$J = \int_S r^3 \, dr \, d\phi$$

stands for moment of inertia of the cross section, l denotes length of the cylinder, and $\vartheta = \alpha l$ is twist angle. Introducing the notation

$$\sigma = \frac{Ml}{J} \tag{22}$$

we arrive at the formula for the stress σ as a function of time t for an arbitrary deformation program $\vartheta(t)$,

$$\sigma(t) = G\left[\vartheta(t) - \kappa \int_0^\infty \Gamma(v) p_a(v) \, dv \times \int_0^t \exp(-\Gamma(v)(t-\tau)) \vartheta(\tau) \, d\tau \right] \tag{23}$$

For a standard relaxation test with

$$\vartheta(t) = \begin{cases} 0, & t < 0 \\ \vartheta^0, & t \geq 0 \end{cases}$$

Equation (23) reads

$$\sigma(t) = \sigma^0 - \sigma^1 \int_0^\infty [1 - \exp(-\Gamma(v)t)] p_a(v) \, dv \tag{24}$$

where

$$\sigma^0 = G\vartheta^0 \tag{25}$$

is the stress at the beginning of the relaxation test, and

$$\sigma^1 = \kappa\sigma^0 \tag{26}$$

Equations (24)–(26) will be used later to approximate the experimental data depicted in Figures 3–5.

BENDING OF A RECTILINEAR BEAM

We proceed with plane bending of a cantilever beam with a constant cross section that has two axes of symmetry. Denote by l length of the beam and by b the characteristic size of its cross-section. We confine ourselves to deformation of slender beams with $l \gg b$.

Points of the beam refer to Cartesian coordinates $\{x, y, z\}$ with unit vectors $\bar{e}_x$, $\bar{e}_y$, and $\bar{e}_z$, where the vector $\bar{e}_x$ is directed along the longitudinal axis of the beam, and the vectors $\bar{e}_y$ and $\bar{e}_z$ are directed along the main axes of symmetry of the cross section. Deformation of the beam occurs in the plane (x, y) under the action of a force $F(t)$ applied to the free end, $x = l$, along the y axis. The other end, $x = 0$, is clamped.

At plain bending of a rectilinear beam, the strain tensor $\hat{\epsilon}$ and the stress tensor $\hat{\sigma}$ are functions of time t, the longitudinal coordinate x, and the transverse coordinate y. According to the first kinematic Kirchhoff hypothesis, the strain tensor reads

$$\hat{\epsilon} = \epsilon_0(t, x, y) \bar{e}_x \bar{e}_x \tag{27}$$

where $\epsilon_0(t, x, y)$ is the longitudinal strain. Substitution of expression (27) into the constitution eq. (17) implies that

$$\hat{\sigma} = \sigma_0(t, x, y) \bar{e}_x \bar{e}_x + \sigma_1(t, x, y)(\bar{e}_y \bar{e}_y + \bar{e}_z \bar{e}_z)$$

where

$$\sigma_0(t, x, y) = -P(t, x, y) + \frac{4}{3} G\left[\epsilon_0(t, x, y) - \kappa \int_0^\infty \Gamma(v) p_a(v) \, dv \int_0^t \exp(-\Gamma(v)(t-\tau)) \epsilon_0(\tau, x, y) \, d\tau \right]$$

$$\sigma_1(t, x, y) = -P(t, x, y) - \frac{2}{3} G\left[\epsilon_0(t, x, y) - \kappa \int_0^\infty \Gamma(v) p_a(v) \, dv \int_0^t \exp(-\Gamma(v)(t-\tau)) \epsilon_0(\tau, x, y) \, d\tau \right] \tag{28}$$

With reference to the static Kirchhoff hypothesis, we set

$$\sigma_1(t, x, y) = 0 \tag{29}$$

It follows from eqs. (28) and (29) that the only nonzero component of the stress tensor, the longitudinal stress σ_0, is given by

$$\sigma_0(t, x, y) = 2G\left[\epsilon_0(t, x, y) - \kappa \int_0^\infty \Gamma(v) p_a(v) \, dv \times \int_0^t \exp(-\Gamma(v)(t-\tau)) \epsilon_0(\tau, x, y) \, d\tau \right] \tag{30}$$

The bending moment $M(t, x)$ is determined by the standard formula

$$M(t, x) = \int_S \sigma_0(t, x, y) y \, dy \, dz \tag{31}$$

where S denotes the domain occupied by the cross section of the beam. At plane bending of a slender beam, the longitudinal strain ϵ_0 reads

$$\epsilon_0(t, x, y) = -y \frac{\partial^2 u}{\partial x^2}(t, x) \tag{32}$$

where $u(t, x)$ is the beam deflection at time $t \geq 0$ at point $x \in [0, l]$. Substitution of eqs. (30) and (32) into eq. (31) implies that

$$M(t, x) = 2GJ\left[\frac{\partial^2 u}{\partial x^2}(t, x) - \kappa \int_0^\infty \Gamma(v)p_a(v)\, dv \times \int_0^t \exp(-\Gamma(v)(t-\tau)) \frac{\partial^2 u}{\partial x^2}(\tau, x)\, d\tau\right] \tag{33}$$

where

$$J = \int_S y^2\, dy\, dz$$

stands for moment of inertia of the cross section. Equating the bending moment M to the moment of the external force F, we arrive at the integrodifferential equation

$$\frac{\partial^2 u}{\partial x^2}(t, x) - \kappa \int_0^\infty \Gamma(v)p_a(v)\, dv \int_0^t \exp(-\Gamma(v)(t-\tau)) \times \frac{\partial^2 u}{\partial x^2}(\tau, x)\, d\tau = \frac{F(t)}{2GJ}(l - x) \tag{34}$$

The boundary conditions at the clamped end of the beam $x = 0$ are given by

$$u(t, 0) = 0, \quad \frac{\partial u}{\partial x}(t, 0) = 0 \tag{35}$$

Integration of eq. (34) with boundary conditions (35) results in

$$u(t, x) - \kappa \int_0^\infty \Gamma(v)p_a(v)\, dv \int_0^t \exp(-\Gamma(v)(t-\tau)) \times u(\tau, x)\, d\tau = \frac{F(t)}{12GJ} x^2(3l - x) \tag{36}$$

Equation (36) determines the deflection of a cantilever beam at an arbitrary point x. Setting $x = l$ in eq. (36), we obtain

$$u(t, l) - \kappa \int_0^\infty \Gamma(v)p_a(v)\, dv \int_0^t \exp(-\Gamma(v)(t-\tau)) \times u(\tau, l)\, d\tau = \frac{F(t)l^3}{2EJ}$$

where

$$E = 3G \tag{37}$$

is an analog of the Young's modulus. Finally, introducing the strain $\epsilon(t) = u(t, l)/l$ and the stress $\sigma(t) = F(t)l^2/(2J)$, we find that

$$\epsilon(t) - \kappa \int_0^\infty \Gamma(v)p_a(v)\, dv \int_0^t \exp(-\Gamma(v)(t-\tau))\epsilon(\tau)\, d\tau = \frac{\sigma(t)}{E} \tag{38}$$

Equation (38) is similar to constitutive eq. (17), where pressure P is dropped, and the stress tensor $\hat{\sigma}$ and the strain tensor $\hat{\epsilon}$ are replaced by σ and ϵ, respectively.

Formula (38) provides the stress–strain relation for an arbitrary loading program. In what follows, we concentrate on a standard creep test with

$$\sigma(t) = \begin{cases} 0, & t < 0 \\ \sigma^0, & t \geq 0 \end{cases}$$

Substitution of this expression into eq. (38) implies that

$$\epsilon(t) = \epsilon^0 + \kappa \int_0^\infty Z(t, v)p_a(v)\, dv \tag{39}$$

where $\epsilon^0 = \sigma^0/E$ is the strain at the beginning of the creep process, and

$$Z(t, v) = \Gamma(v) \int_0^t \exp(-\Gamma(v)(t-\tau))\epsilon(\tau)\, d\tau$$

Differentiating this equality with respect to time, we find that the function $Z(t, v)$ is governed by the differential equation

$$\frac{\partial Z}{\partial t}(t, v) = \Gamma(v)[\epsilon(t) - Z(t, v)], \quad Z(0, v) = 0 \tag{40}$$

Equations (39) and (40) will be employed later to match observations in bending creep tests.

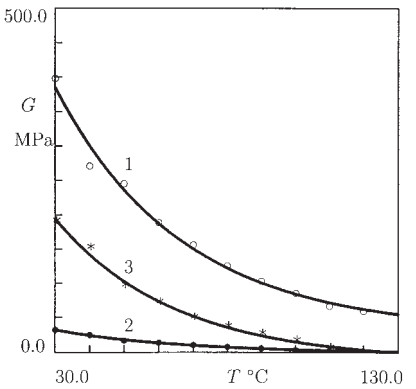

Figure 6 The modulus G versus temperature T. Symbols: treatment of observations in relaxation tests on iPP (unfilled circles), LDPE (filled circles), and LLDPE (asterisks). Solid lines: approximation of the experimental data by eq. (41). Curve 1: $G_0 = 32.30$, $G_1 = 799.42$, $T_0 = 36.6$. Curve 2: $G_0 = -1.59$, $G_1 = 764.92$, $T_0 = 36.5$. Curve 3: $G_0 = -11.54$, $G_1 = 496.47$, $T_0 = 34.0$.

FITTING OBSERVATIONS IN RELAXATION TESTS

The aim of this section is to find adjustable parameters G, γ, V, Σ, and κ in the governing equations (2), (6), and (24)–(26) by fitting the experimental data in torsion relaxation tests depicted in Figures 3–5. Each relaxation curve is approximated separately. To find the quantities γ, V, and Σ, we fix some intervals $[0, \gamma_{max}]$, $[0, V_{max}]$, and $[0, \Sigma_{max}]$, where the best fit parameters γ, V, and Σ are assumed to be located, and divide these intervals into J subintervals by the points $\gamma^{(i)} = i\Delta\gamma$, $V^{(j)} = j\Delta V$, and $\Sigma^{(k)} = k\Delta\Sigma$ ($i, j, k = 1, \ldots, J - 1$) with $\Delta\gamma = \gamma_{max}/J$, $\Delta V = V_{max}/J$, and $\Delta\Sigma = \Sigma_{max}/J$. For any pair $\{V^{(j)}, \Sigma^{(k)}\}$, the coefficient p_0 in eq. (6) is found from condition (7), where the integral is calculated numerically by Simpson's method with 300 points and the step $\Delta v = 0.1$. For any triad $\{\gamma^{(i)}, V^{(j)}, \Sigma^{(k)}\}$, the integral in eq. (24) is evaluated numerically. The coefficients σ^0 and σ^1 are determined by the least-squares technique from the condition of minimum of the function

$$R = \sum_{t_m} [\sigma_{exp}(t_m) - \sigma_{num}(t_m)]^2$$

where the sum is calculated over all times t_m at which observations are depicted in Figures 3–5, σ_{exp} is the stress measured in a relaxation test, and σ_{num} is given by eqs. (24). The parameters γ, V, and Σ are determined from the condition of minimum of the function R on the set $\{\gamma^{(i)}, V^{(j)}, \Sigma^{(k)}$ ($i, j, k = 1, \ldots, J - 1$)$\}$. After finding the best fit values $\gamma^{(i)}$, $V^{(j)}$, and $\Sigma^{(k)}$, this procedure is repeated twice for the new intervals $[\gamma^{(i-1)}, \gamma^{(i+1)}]$, $[V^{(j-1)}, V^{(j+1)}]$, and $[\Sigma^{(k-1)}, \Sigma^{(k+1)}]$, to ensure an acceptable accuracy of fitting. When the best fit values of γ, V, and Σ are found, the material constants G and κ are calculated by formulas (25) and (26). Figures 3–5 demonstrate excellent agreement between the observations in relaxation tests and the results of numerical simulation.

The modulus G is plotted versus temperature T in Figure 6. The experimental data are approximated by the phenomenological relation

$$G = G_0 + G_1 \exp\left(-\frac{T}{T_0}\right) \tag{41}$$

where T_0 is some characteristic temperature. Given T_0, the coefficients G_m ($m = 0, 1$) in eq. (41) are found by the least-squares method. The temperature T_0 is determined by the steepest-descent algorithm. Figure 6 shows that eq. (41) provides good quality of matching the experimental data.

The attempt rate γ is plotted versus the absolute temperature T in Figure 7. To approximate the observations, we employ the Arrhenius equation

$$\gamma = \gamma_0 \exp\left(-\frac{\Delta H}{RT}\right) \tag{42}$$

where R is the universal gas constant, ΔH is an activation energy, and γ_0 is the attempt rate at high temperatures ($T \to \infty$). To match the experimental data, it is convenient to rewrite eq. (42) in the form

$$\ln \gamma = g_0 - \frac{g_1}{T} \tag{43}$$

with

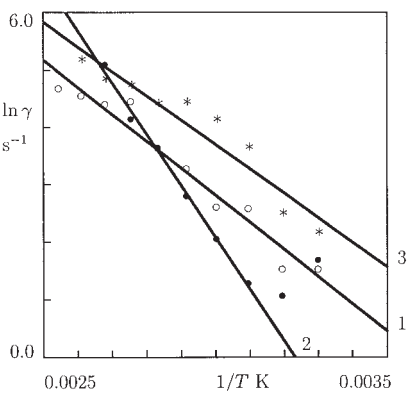

Figure 7 The attempt rate γ versus temperature T. Symbols: treatment of observations in relaxation tests on iPP (unfilled circles), LDPE (filled circles), and LLDPE (asterisks). Solid lines: approximation of the experimental data by eq. (43). Curve 1: $\gamma_0 = 16.97$, $\gamma_1 = 4.72 \times 10^3$. Curve 2: $\gamma_0 = 29.15$, $\gamma_1 = 9.02 \times 10^3$. Curve 3: $\gamma_0 = 16.49$, $\gamma_1 = 4.26 \times 10^3$.

TABLE II
Activation Energies ΔH of Semicrystalline Polymers

Polymer	ΔH (kcal/mol)	Literature data	Source
iPP	9.5	7.3	[54]
		9.2	[55]
LDPE	17.9	12.7	[56]
		13.5	[57]
		25.0	[58]
LLDPE	8.5	7.3	[57]
		7.8	[56]

$$g_0 = \ln \gamma_0, \quad g_1 = \frac{\Delta H}{R} \tag{44}$$

The coefficients g_m ($m = 0, 1$) in eq. (43) are found by the least-squares technique. Figure 7 demonstrates that eq. (43) correctly describes the observations for three semicrystalline polymers (the only exception is the experimental points for LDPE at low temperatures $T = 30$ and 40°C). After determining the best fit adjustable parameters g_m, the activation energy ΔH is calculated according to eq. (44). The values of ΔH are collected in Table II.

The dimensionless average activation energy for rearrangement of strands V and the dimensionless standard deviation of activation energies Σ are plotted versus temperature T in Figures 8 and 9. The experimental data are approximated by the linear dependencies

$$V = V_0 + V_1 T, \quad \Sigma = \Sigma_0 + \Sigma_1 T \tag{45}$$

where the coefficients V_m and Σ_m ($m = 0, 1$) are determined by the least-squares algorithm. These figures reveal that eqs. (45) adequately describe the effect of temperature on the adjustable parameters V and Σ for all three polyolefins.

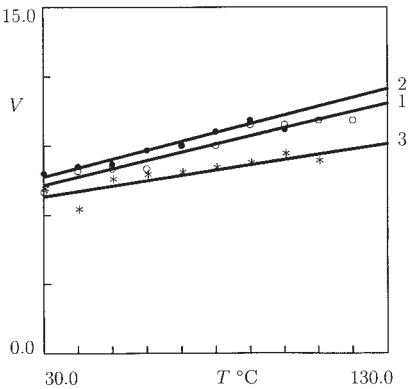

Figure 8 The average activation energy V versus temperature T. Symbols: treatment of observations in relaxation tests on iPP (unfilled circles), LDPE (filled circles), and LLDPE (asterisks). Solid lines: approximation of the experimental data by eqs. (45). Curve 1: $V_0 = 6.23$, $V_1 = 3.55 \times 10^{-2}$. Curve 2: $V_0 = 6.51$, $V_1 = 3.82 \times 10^{-2}$. Curve 3: $V_0 = 6.11$, $V_1 = 2.28 \times 10^{-2}$.

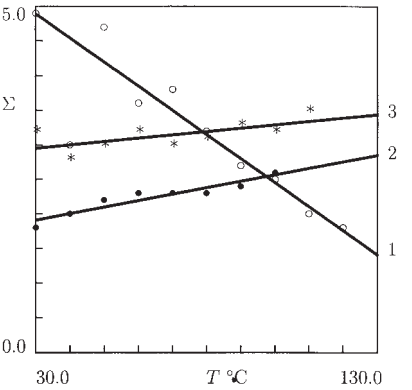

Figure 9 The standard deviation of activation energies Σ versus temperature T. Symbols: treatment of observations in relaxation tests on iPP (unfilled circles), LDPE (filled circles), and LLDPE (asterisks). Solid lines: approximation of the experimental data by eqs. (45). Curve 1: $\Sigma_0 = 5.94$, $\Sigma_1 = -3.48 \times 10^{-2}$. Curve 2: $\Sigma_0 = 1.63$, $\Sigma_1 = 9.40 \times 10^{-3}$. Curve 3: $\Sigma_0 = 2.81$, $\Sigma_1 = 4.83 \times 10^{-3}$.

The concentration of active MRs κ is plotted versus temperature T in Figure 10. The experimental data are matched by the linear function

$$\kappa = \kappa_0 + \kappa_1 T \tag{46}$$

where the coefficients κ_m ($m = 0, 1$) are found by the least-squares method. According to Figure 10, eq. (46) correctly predicts changes in the concentration of active mesodomains with temperature.

DISCUSSION

Figure 6 shows that the modulus G monotonically decreases with temperature T. For all polymers under

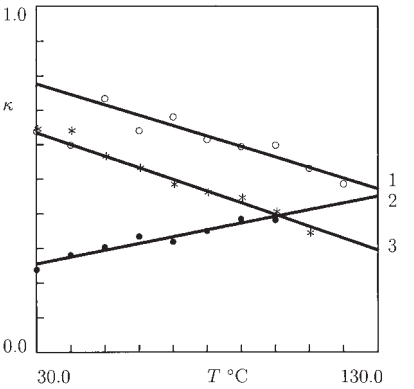

Figure 10 The concentration of active MRs κ versus temperature T. Symbols: treatment of observations in relaxation tests on iPP (unfilled circles), LDPE (filled circles), and LLDPE (asterisks). Solid lines: approximation of the experimental data by eq. (46). Curve 1: $\kappa_0 = 0.87$, $\kappa_1 = -3.04 \times 10^{-3}$. Curve 2: $\kappa_0 = 0.20$, $\kappa_1 = 1.95 \times 10^{-3}$. Curve 3: $\kappa_0 = 0.74$, $\kappa_1 = -3.38 \times 10^{-3}$.

consideration, the reduction in the elastic modulus is correctly approximated by the exponential dependence (41). Given a temperature T, the modulus of iPP exceeds that for LLDPE, whereas the latter is higher than the modulus of LDPE. The fact that the modulus of LLDPE exceeds that of LDPE is in agreement with the DSC data reported in Table I, which demonstrate that the degree of crystallinity of LLDPE is higher than that of LDPE by a factor of 1.8. The latter implies that the modulus of LLDPE should exceed that of LDPE, because the rigidity of crystallites is substantially higher than that of amorphous rubbery regions.

The elastic moduli of polyethylenes vanish in the interval of temperatures between 110 and 140°C, that is, in the close vicinity of the melting temperatures T_m of these polymers. Based on this result, we can present eq. (41) in the form

$$G = G_*\left[\exp\left(\frac{T_m - T}{T_0}\right) - 1\right]$$

with only two material constants G_* and T_0.

The characteristic temperature T_0 that describes the decrease in G with temperature is practically independent of the crystalline morphology and the degree of branching of chains (for all polymers, T_0 lies in the interval between 34 and 37°C). The ratio

$$\zeta = \frac{G_1}{G_0 + G_1}$$

that characterizes the rate of reduction in the modulus with temperature, is also practically independent of the chemical structure of polymers ($\zeta = 0.96$ for iPP, $\zeta = 1.00$ for LDPE, and $\zeta = 1.02$ for LLDPE).

To validate our findings, we compare the modulus of iPP at room temperature ($T = 20$°C) given by eq. (41) with that provided by the supplier. The difference between the calculated value $G = 0.495$ GPa and that determined in terms of the flexural modulus reported by the supplier and recalculated with the help of eq. (37) $G = 0.529$ GPa does not exceed 6%.

Appropriate deviations for LDPE (25.8%) and LLDPE (33.9%) are noticeably higher, but we use secant moduli indicated by the suppliers instead of the Young's moduli that are unavailable. To confirm that this explanation for the discrepancies is reasonable, we compare the elastic modulus of LDPE found in the present paper with that determined in uniaxial tensile tests with various strain rates in our recent study.[59] The shear modulus corresponding to the strain rate 1.0 s^{-1} determined in that work (based on another constitutive model that accounts for the viscoplastic behavior of a semicrystalline polymer and neglects rearrangement of strands in an equivalent network) equals 41.18 MPa, which is extremely close to the value $G = 42.6$ MPa found in the present paper (the difference is less than 4%).

Figure 7 demonstrates that the attempt rate γ monotonically increases with temperature T for all polymers under consideration. The growth of the attempt rate is correctly described by the Arrhenius dependence (43), which confirms our assumption that rearrangement of strands in an equivalent network is thermally activated. According to Table II, the activation energies ΔH found by matching our experimental data are in good agreement with those reported by other researchers.

Figure 8 reveals that the average activation energies V of three semicrystalline polymers slightly increases with temperature. The rate of this growth is practically independent of the crystalline morphology of the polymers: the coefficient V_1 in eqs. (45) equals 3.6×10^{-2} for iPP, 3.8×10^{-2} for LDPE, and 2.38×10^{-2} for LLDPE. Given a temperature T, the highest value of V is found for LDPE, and the lowest value of V is found for LLDPE.

The increase in the activation energy with temperature may be attributed to reconstruction of crystallites and smectic mesophase under heating. Some tie chains that bridge lamellar blocks in the stacks at room temperature are broken with an increase in T, and the detached blocks diffuse into the amorphous phase, where they serve as extra crosslinks with high activation energies.

It follows from Figure 9 that the crystalline morphology of iPP changes with temperature in a different way than the morphology of polyethylenes. The standard deviation of activation energies Σ (which may be treated as a measure of heterogeneity of an equivalent network of strands) strongly decreases with temperature for iPP and increases for LDPE and LLDPE. This difference may be explained by partial reconstruction of smectic mesophase in iPP under heating. This transformation reduces the difference between the activation energies of strands belonging to mesoregions located in the bulk amorphous phase and in the close vicinities of crystallites. As a result, the level of spatial heterogeneity of the network is diminished, which is reflected by the model as a decrease in Σ with temperature.

On the contrary, heating of LDPE and LLDPE (especially in the submelting region) causes melting of lamellae. Partial melting of crystallites induces separation of lamellar blocks from their stacks. The separated blocks move into the amorphous phase where they serve as extra physical crosslinks. As the activation energies for detachment of tie chains from the surfaces of these blocks differ substantially from the activation energies for rearrangement of chains in the amorphous phase, the spatial inhomogeneity of the network grows, which is observed as an increase in Σ with T. The coefficient Σ_1 in eqs. (45) that characterizes

the increase in the standard deviation of activation energies with temperature is larger (by about twice) for LDPE ($\Sigma_1 = 9.4 \times 10^{-3}$) than for LLDPE ($\Sigma_1 = 4.8 \times 10^{-3}$). This conclusion seems quite natural, because lamellar stacks in LDPE are less rigid compared to LLDPE (due to the presence of long-chain branches). The latter is confirmed by Raman spectroscopy, see Figure 6 in [6].

Figure 10 demonstrates that the concentration of active mesoregions κ increases with temperature for LDPE and decreases for iPP and LLDPE. An increase in κ of LDPE with temperature appears natural (in particular, in the submelting region of temperatures), and it may be ascribed to release of the rigid amorphous fraction (chains in the amorphous regions whose mobility is restricted by surrounding crystallites) driven by partial melting of crystallites.

The observed reduction in the concentration of active amorphous regions in iPP with temperature may be attributed to rearrangement (partial recrystallization) of smectic mesophase (interfacial and mobile crystalline phases according to the classification proposed in [60]) in the close neighborhoods of lamellar blocks, which results in immobilization of chains in amorphous regions surrounded by radial and transverse lamellae.

A similar explanation may be proposed for the decrease in κ with temperature found for LLDPE: a pronounced decrease in the mass fraction of the interfacial phase and mobile crystalline phase due to their rearrangement that induces immobilization of chains in surrounding amorphous regions. Our hypothesis is confirmed by comparison of the experimental data for LLDPE depicted in Figure 10 with the observations reported in Figure 3 of ref. [60]. According to Figure 10, the concentration of active mesodomains at room temperature $\kappa = 0.63$, which corresponds to the total content of rubbery, interfacial and mobile crystalline phases determined in [60]. At the temperature $T = 100$°C, the concentration of active MRs decreases to $\kappa = 0.30$, which roughly corresponds to the mass fraction of the rubbery phase reported in [60]. The latter means that polymer chains in the interfacial and mobile crystalline domains that are active at room temperature become immobilized with the growth of T due to partial recrystallization of smectic mesophase.

The same phenomenon (partial immobilization of chains in the rubbery domains) should also take place in LDPE. It is, however, noticeably less pronounced in LDPE compared with LLDPE, where the distribution of crystal sizes is substantially more heterogeneous due to a wide distribution of side groups along and across polymer chains [6].

It is worth noting that the rates of decrease in κ with temperature for iPP and LLDPE specimens practically coincide: the coefficient κ_1 in eq. (46) equals -3.0×10^{-3} for iPP and -3.4×10^{-3} for LLDPE. We treat, however, this similarity as coincidental, due to the substantial difference in crystalline morphologies of these polymers.

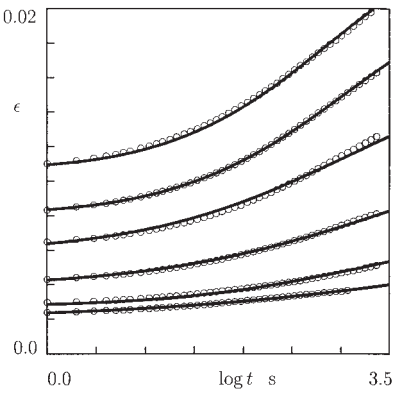

Figure 11 The strain ϵ versus time t. Circles: experimental data on iPP in tensile creep tests at the temperatures $T = 30$, 40, 60, 80, 100, and 120°C from bottom to top, respectively. Solid lines: predictions of the model.

VALIDATION OF THE MODEL

It has been demonstrated by matching the relaxation curves that (1) the constitutive equations correctly describe the experimental data in relaxation tests, and (2) the adjustable parameters found by fitting the observations change with temperature in a physically plausible way. The question arises, however, whether the model can adequately predict observations in mechanical tests.

To validate the stress–strain relations, a series of six creep tests was performed on injection-molded iPP specimens at the temperatures $T = 30$, 40, 60, 80, 100, and 120°C. The tests were carried out on the dynamic mechanical analyzer DMTA V (Rheometric Scientific Co.) in the cantilever bending mode. To avoid the effect of physical aging, mechanical tests were performed a few days after preparation of samples.

In each creep test, a specimen was equilibrated at a given temperature T (for 10 min). Afterwards, the specimen was loaded up to a given stress $\sigma = 1.0$ MPa (within 15 s). The stress remained constant during the creep time $t_c = 40$ min, and the strain was measured by using a standard extensometer. At each temperature, at least two creep tests were conducted on different samples.

The strain ϵ is plotted versus the logarithm of time t in Figure 11 (the initial instant $t = 0$ corresponds to the beginning of the creep process). This figure demonstrates that the increase in strain is rather modest at relatively low temperatures (30 and 40°C), but it becomes more pronounced at higher temperatures.

Each creep curve in Figure 11 is approximated separately by using the quantities V, Σ, and κ found by matching the experimental data depicted in Figure 3. The coefficient p_0 in eq. (6) is found from condition (7), where the integral is calculated numerically by Simpson's method with 300 points and the step $\Delta v = 0.1$. The initial strain ϵ^0 equals the strain measured at the beginning of a creep test. To ensure good fit of the creep curves, we treat the attempt rate γ as an adjustable parameter. To find this quantity, we fix an interval $[0, \gamma_{max}]$, where the best fit value of γ is assumed to be located, and divide this interval into J subintervals by the points $\gamma^{(i)} = i\Delta\gamma$ ($i = 1, \ldots, J - 1$) with $\Delta\gamma = \gamma_{max}/J$. For each $\gamma^{(i)}$, the integral in eq. (38) is evaluated by Simpson's method with 300 points and the step $\Delta v = 0.1$. Differential equation (39) is solved numerically by the Runge–Kutta method with the time-step $\Delta t = 0.03$ s. The attempt rate γ is determined from the condition of minimum of the function

$$R = \sum_{t_m} [\epsilon_{exp}(t_m) - \epsilon_{num}(t_m)]^2$$

on the set $\{\gamma^{(i)} (i = 1, \ldots, J - 1)\}$. The sum is calculated over all times t_m at which observations are reported in Figure 11; ϵ_{exp} is the strain measured in a creep test, and ϵ_{num} is given by eq. (38). After finding the best fit value $\gamma^{(i)}$, this procedure is repeated twice for the new intervals $[\gamma^{(i-1)}, \gamma^{(i+1)}]$, to provide an acceptable accuracy of fitting.

Figure 11 demonstrates excellent agreement between the observations in creep tests and the results of numerical simulation at all temperatures, but $T = 80$°C, at which some deviations are observed between the experimental data and the numerical results.

The attempt rate γ is plotted versus temperature T in Figure 12. The experimental data are approximated by the Arrhenius eq. (43), where the coefficients g_m ($m = 0, 1$) are found by the least-squares technique. Figure 12 shows that eq. (43) correctly fits the observations. The activation energies ΔH determined by matching creep and relaxation curves are extremely close to one another: $\Delta H = 9.19$ kcal/mol for creep tests, and $\Delta H = 9.37$ kcal/mol for relaxation tests (the difference is less than 2%). At all temperatures under consideration, the attempt rate determined in the approximation of creep curves slightly exceeds that found by fitting relaxation curves. However, we treat the difference between curves 1 and 2 in Figure 12 as insignificant, because it is less than the scatter of experimental data around the curves. Based on this finding, we conclude that the constitutive equations can correctly predict observations in creep tests, when the material constants are found by matching experimental data in relaxation tests.

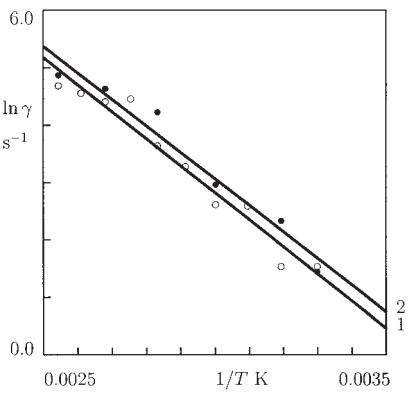

Figure 12 The attempt rate γ versus temperature T. Symbols: treatment of observations in relaxation (unfilled circles) and creep (filled circles) tests on iPP. Solid lines: approximation of the experimental data by eq. (43). Curve 1: $\gamma_0 = 16.97$, $\gamma_1 = 4.72 \times 10^3$. Curve 2: $\gamma_0 = 16.93$, $\gamma_1 = 4.62 \times 10^3$.

CONCLUSION

Three series of torsional relaxation tests were performed on injection-molded iPP, LDPE, and LLDPE in the range of temperatures from room temperature to $T = 120$°C.

A constitutive model was derived for the viscoelastic response of semicrystalline polymers at small strains. A polymer is treated as an equivalent transient network of strands bridged by temporary junctions. Active strands separate from their junctions at random instants as they are activated by thermal fluctuations. Dangling strands merge with nearby junctions at random times. The equivalent network is treated as an ensemble of mesoregions with various activation energies for rearrangement of strands.

Constitutive equations are derived by using the laws of thermodynamics. The stress–strain relations involve five adjustable parameters that are found by fitting the experimental data. Good agreement is demonstrated between the observations in relaxation tests and the results of numerical simulation. It is also revealed that the governing equations can correctly predict experimental data in bending creep tests on iPP, when the material constants are determined by fitting data in torsional relaxation tests.

The following conclusions are drawn:

1. The elastic modulus G monotonically decreases with temperature following the exponential law (41). The characteristic temperature T_0 for the decay in the modulus with temperature is independent of the crystalline morphology of the polymers.
2. The attempt rate for rearrangement of strands γ increases with temperature T following the Arrhenius dependence (42). The activation energies ΔH found by matching relaxation curves are close to those determined by other researchers.

3. The average activation energy V slightly increases with temperature in accord with linear eq. (45). The rate of increase in V is practically independent of the crystalline structure of polyolefins.
4. The standard deviation of activation energies Σ and the concentration of active mesoregions κ are strongly affected by the crystalline morphology.
5. The parameter Σ decreases with temperature for iPP and increases with T for polyethylenes. The decrease in Σ with temperature is explained by partial reconstruction of smectic mesophase under heating, which results in homogenization of the ensemble of MRs. The increase in Σ with T is ascribed to detachment of lamellar blocks from their stacks and their diffusion into the amorphous phase, where the separated blocks serve as extra physical crosslinks with high activation energies.
6. The concentration of active mesodomains κ increases with temperature for LDPE and decreases for iPP and LLDPE. The observed growth of κ is attributed to the release of the rigid amorphous fraction driven by partial melting of crystallites. The decrease in κ with temperature is associated with rearrangement of the interfacial and mobile crystalline domains, which results in immobilization of chains in smectic mesophase.

This work was partially supported by the West Virginia Research Challenge Grant Program.

References

1. Iijima, M.; Strobl, G. Macromolecules 2000, 33, 5204.
2. Kalay, G.; Bevis, M. J. J Polym Sci, Part B: Polym Phys 1997, 35, 241, 265.
3. Silvestre, C.; Cimmino, S.; Triolo, R. J Polym Sci, Part B: Polym Phys 2003, 41, 493.
4. Maiti, P.; Hikosaka, M.; Yamada, K.; Toda, A.; Gu, F. Macromolecules 2000, 33, 9069.
5. Coulon, G.; Castelein, G.; G'Sell, C. Polymer 1998, 40, 95.
6. Lagaron, J. M. J Mater Sci 2002, 37, 4101.
7. Kazimerczak, T.; Galeski, A. J Appl Polym Sci 2002, 85, 1337.
8. Graham, J. T.; Alamo, R. G.; Mandelkern, L. J Polym Sci, Part B: Polym Phys 1997, 35, 213.
9. Matsuda, H.; Aoike, T.; Uehara, H.; Yamanobe, T.; Komoto, T. Polymer 2001, 42, 5013.
10. Tian, M.; Loos, J. J Polym Sci, Part B: Polym Phys 2001, 39, 763.
11. Lue, J.; Sue, H.-J. J Polym Sci, Part B: Polym Phys 2002, 40, 507.
12. Guichon, O.; Seguela, R.; David, L.; Vigier, G. J Polym Sci, Part B: Polym Phys 2003, 41, 327.
13. Teng, H.; Shi, Y.; Jin, X. J Polym Sci, Part B: Polym Phys 2002, 40, 2107.
14. Verma, R.; Marand, H.; Hsiao, B. Macromolecules 1996, 29, 7767.
15. Kruczala, K.; Varghese, B.; Bokria, J. G.; Schlick, S. Macromolecules 2003, 36, 1899.
16. Ariyama, T.; Mori, Y.; Kaneko, K. Polym Eng Sci 1997, 37, 81.
17. Dutta, N. K.; Edward, G. H. J Appl Polym Sci 1997, 66, 1101.
18. Read, B. E.; Tomlins, P. E. Polymer 1997, 38, 4617.
19. Tomlins, P. E.; Read, B. E. Polymer 1998, 39, 355.
20. Sweeney, J.; Collins, T. L. D.; Coates, P. D.; Duckett, R. A. J Appl Polym Sci 1999, 72, 563.
21. Yamaguchi, M.; Nitta, K.-H.; Tanaka, A.; Kitamura, M. J Polym Sci, Part B: Polym Phys 1999, 37, 1513.
22. Drozdov, A. D.; Christiansen, J. deC. Macromol Theory Simul 2002, 11, 884.
23. Drozdov, A. D.; Christiansen, J. deC. Polym Eng Sci 2003, 43, 946.
24. Chengalva, M. K.; Kenner, V. H.; Popelar, C. H. Int J Solids Struct 1995, 32, 847.
25. Lai, J.; Bakker, A. Polymer 1995, 36, 93.
26. Rand, J. L.; Henderson, J. K.; Grant, D. A. Polym Eng Sci 1996, 36, 1058.
27. Lee, H.; Cho, K.; Ahn, T.-K.; Choe, S.; Kim, I.-J.; Park, I.; Lee, B. H. J Polym Sci, Part B: Polym Phys 1997, 35, 1633.
28. Zhang, C.; Moore, I. D. Polym Eng Sci 1997, 37, 404.
29. Zhou, H.; Wilkes, G. L. Polymer 1998, 39, 3597.
30. Bonner, M.; Duckett, R. A.; Ward, I. M. J Mater Sci 1999, 34, 1885.
31. Meyer, R. W.; Pruitt, L. A. Polymer 2001, 42, 5293.
32. Ohta, Y.; Kaji, A.; Sugiyama, H.; Yasuda, H. J Appl Polym Sci 2001, 81, 312.
33. Hubert, L.; David, L.; Seguela, R.; Vigier, G.; Corfias-Zuccalli, C.; Germain, Y. J Appl Polym Sci 2002, 84, 2308.
34. Drozdov, A. D.; Yuan, Q. Int J Solids Struct 2003, 40, 2321.
35. O'Connell, P. A.; Bonner, M. J.; Duckett, R. A.; Ward, I. M. J Appl Polym Sci 2003, 89, 1663.
36. Berström, J. S.; Kurtz, S. M.; Rimnac, C. M.; Edidin, A. A. Biomaterials, 23, 2002, 2329.
37. Bensason, S.; Stepanov, E. V.; Chum, S.; Hiltner, A.; Baer, E. Macromolecules 1997, 30, 2436.
38. Chang, A.; Cheung, Y. W.; Hiltner, A.; Baer, E. J Polym Sci, Part B: Polym Phys 2002, 40, 142.
39. Sabbagh, A. B.; Lesser, A. J. J Polym Sci, Part B: Polym Phys 1999, 37, 2651.
40. Green, M. S.; Tobolsky, A. V. J Chem Phys 1946, 14, 80.
41. Yamamoto, M. J Phys Soc Japan 1956, 11, 413.
42. Lodge, A. S. Rheol Acta 1968, 7, 379.
43. Tanaka, F.; Edwards, S. F. Macromolecules 1992, 25, 1516.
44. Drozdov, A. D.; Christiansen, J. deC. Comput Mater Sci 2003, 27, 403.
45. Androsch, R.; Wunderlich, B. Macromolecules 2001, 34, 5950.
46. Dai, P. S.; Cebe, P.; Capel, M.; Alamo, R. G.; Mandelkern, L. Macromolecules 2003, 36, 4042.
47. Wunderlich, B. Crystal Melting; in Macromolecular Physics; Academic Press: New York, 1980; Vol. 3.
48. Al-Hussein, M.; Davies, G. R.; Ward, I. M. J Polym Sci, Part B: Polym Phys 2000, 38, 755–764.
49. Drummond, K. M.; Shanks, R. A.; Cser, F. J Appl Polym Sci 2002, 83, 777–784.
50. Somani, R. H.; Hsiao, B. S.; Nogales, A.; Fruitwala, H.; Srinivas, S.; Tsou, A. H. Macromolecules 2001, 34, 5902–5909.
51. Li, L.; de Jeu, W. H. Macromolecules 2003, 36, 4862–4867.
52. Bouchaud, J.-P., Cugliandolo, L. F.; Kurchan, J.; Mezard, M. in Spin Glasses and Random Fields; Young, A. P., Ed.; World Scientific: Singapore, 1998; p. 161.
53. Derrida, B. Phys Rev Lett 1980, 45, 79.
54. Lopez Manchado, M. A.; Biagiotti, J.; Kenny, J. M. J Appl Polym Sci 2001, 81, 1.
55. Eckstein, A.; Suhm, J.; Friedrich, C.; Maier, R.-D. Macromolecules 1998, 31, 1335.
56. Yamaguchi, M.; Abe, S. J Appl Polym Sci 1999, 74, 3153, 3160.
57. Qui, X.; Ediger, M. D. J Polym Sci, Part B: Polym Phys 2000, 38, 2634–2643.
58. Suehiro, S.; Yamada, T.; Inagaki, H.; Kyu, T.; Nomura, S.; Kawai, H. J Polym Sci: Polym Phys Ed 1979, 17, 763.
59. Drozdov, A. D.; Gupta, R. K. Int J Solids Struct 2003, 40, 6217.
60. Kuwabara, K.; Kaji, H.; Horii, F. Macromolecules 2000, 33, 4453.